Mars Methane Sources in Northwestern Gale Crater Inferred from Back-Trajectory Modeling

Enter authors here: Y. Luo[1], M. A. Mischna[2], J. C. Lin[3], B. Fasoli[3], X. Cai[4], and Y. L. Yung[1,2]

[1]Division of Geological and Planetary Sciences, California Institute of Technology, Pasadena, CA 91125, USA

[2]Jet Propulsion Laboratory, California Institute of Technology, Pasadena, CA 91109, USA

[3]Department of Atmospheric Sciences, University of Utah, Salt Lake City, UT 84112, USA

[4]Santiago High School, Corona, CA 92881, USA

Corresponding author: Y. Luo (yc.luo@caltech.edu)

Key Points:

- Back-trajectory analyses are performed for the methane spikes detected by the Mars Science Laboratory at Gale crater.
- Upstream emission regions are mapped out at unprecedented spatial resolutions.
- Provided a 330-year methane lifetime, the emission site(s) must be located next to the *Curiosity* rover in northwestern Gale crater.

Abstract

During its five years of operation as of 2017, the Sample Analysis at Mars (SAM) Tunable Laser Spectrometer (TLS) on board the *Curiosity* rover has detected six methane spikes above a low background abundance in Gale crater. The methane spikes are likely sourced by nearby emission from the surface. Here we use inverse Lagrangian modeling techniques to identify upstream emission regions on the Martian surface for these methane spikes at unprecedented spatial resolutions. Inside Gale crater, the northwestern crater floor casts the strongest influence on the detections. Outside Gale crater, the upstream regions extend towards the north. The contrasting results from two consecutive TLS methane measurements point to an active emission site to the west and the southwest of the *Curiosity* rover on the northwestern crater floor. The observed spike magnitude and frequency also favor emission sites on the northwestern crater floor, unless there are fast methane removal mechanisms at work, or either the TLS methane spikes or the Trace Gas Orbiter (TGO) non-detections can not be trusted.

1 Introduction

Almost all of the methane in the present-day Earth's atmosphere can be traced back to biological origins (Cicerone and Oremland, 1988). Extending this observation to Mars, this would suggest that the presence of methane in the Martian atmosphere could be a biosignature on this seemingly lifeless planet (Yung et al., 2018). Alternative, abiotic methane production mechanisms on Mars invoke past or present geological activity (reviewed in Oehler and Etiope, 2017) such as serpentinization (Oze and Sharma, 2005), which indicates the presence of liquid water, an indispensable ingredient for life. Abundant methane in the ancient Martian atmosphere could also provide a solution to the conflict between the Faint Young Sun and a warm surface suggested by fluvial and lacustrine features on Mars (e.g., Kite et al., 2017).

In the past two decades, the significance of methane in the Martian atmosphere has motivated a number of remote sensing observations aimed at retrieving the methane abundance in the Martian atmosphere and mapping out its spatial distribution. They reported inconsistent and highly variable methane concentrations (Krasnopolsky et al., 2004; Formisano et al., 2004; Geminale et al., 2008; Mumma et al., 2009; Fonti and Marzo, 2010; Krasnopolsky, 2012; Aoki et al., 2018; Giuranna et al., 2019). To overcome the technical challenges faced by remote sensing observations, the Tunable Laser Spectrometer (TLS; Mahaffy et al., 2012) on board the *Curiosity* rover was sent to Gale crater to make *in situ* measurements. During 4.6 years of operation as of May 2017, twenty direct-ingest measurements and ten enrichment measurements (refer to Webster et al. (2015) and Webster et al. (2018) for the descriptions for the two measurement types) revealed a baseline level of ~0.41 parts-per-billion-by-volume (ppbv), with episodic spikes up to ~10 ppbv (Webster et al., 2018) as summarized in Fig. 1. These spikes have been interpreted as discrete methane emission events (Webster et al., 2015, 2018). Notably, a methane spike with an unprecedently high magnitude, 20.5 ppbv, was announced very recently in Webster et al. (2021). It was the first time that a methane spike had been detected in an enrichment measurement, with a low signal-to-noise ratio of ~5, thus adding to the credibility of the previous methane spikes. Concurrently, the ExoMars Trace Gas Orbiter (TGO) has made solar occultation measurements for the methane concentration in the mid- to high-altitudes. However, it has reported stringent upper limits down to 0.02 ppbv (Korablev et al., 2019; Knutsen et al., 2021; Montmessin et al., 2021). Assuming methane is a long-lived species with a 330-year lifetime as indicated by standard photochemical models (Lefèvre and Forget, 2009), it will be uniformly mixed throughout the Martian atmosphere, so TGO's stringent upper limits obtained in a few detections has been interpreted as the upper limit for methane concentration in the entire

atmosphere, which is then contradictory to TLS's significantly more elevated ~0.41 ppbv background level. Some mechanisms have been proposed to reconcile this inconsistency. TLS performed all its measurements in the near-surface planetary boundary layer (PBL), and methane, if released from the surface, could accumulate in the shallow nighttime PBL (Moores et al., 2019a, 2019b). Some speculative fast removal mechanisms that can possibly cause temporal and spatial inhomogeneity of methane concentration have also been proposed (Gough et al., 2010; Knak Jensen et al., 2014; Hu et al., 2016), which may also potentially reconcile the inconsistency between the TLS and the TGO results. In this study, we first accept both the results from TLS and TGO, and investigate the circumstances in which their discrepancies can be reconciled. We will later re-evaluate the probability of these circumstances.

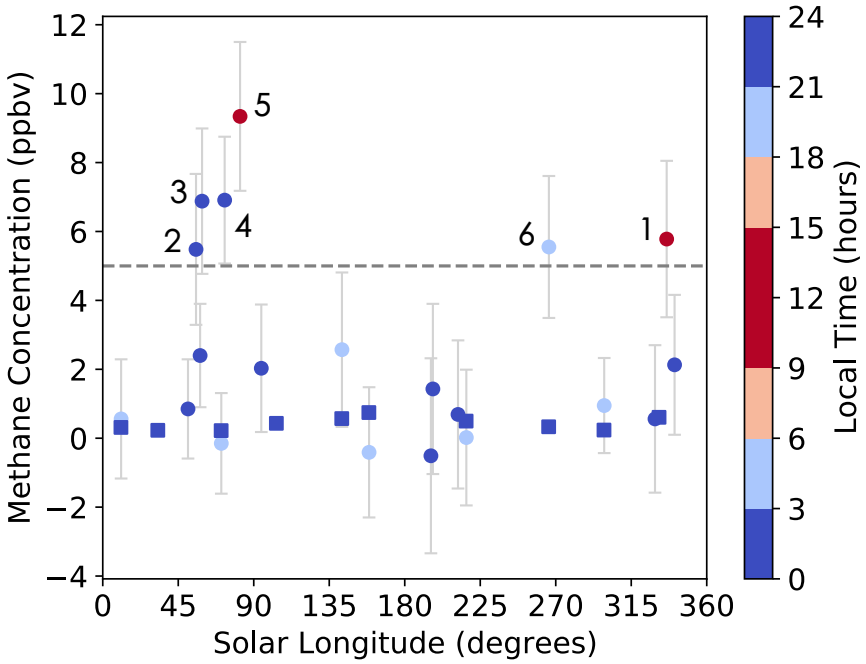

Figure 1. TLS methane signals versus Mars season and local time. The six data points above the horizontal dashed line at 5 ppbv are regarded as the "methane spikes" with their indices labelled next to them. The twenty-four data points below the dashed line are regarded as the

78 background abundance. All the measurements were made in the nighttime except Spikes 1 and 5,
79 which were measured in the early afternoon. Direct-ingest measurements are shown in circles.
80 Enrichment measurements are shown in squares. Colors show the local time of ingestions. Error
81 bars show ±1 standard error of the mean for each measurement. Adapted from Webster et al.
82 (2018).

83 Assuming the existence of methane on Mars is real, its origin will have great implications
84 for geology and astrobiology. The identification of the methane origin requires that we first find
85 the surface emission sites, results from which can inform future missions of high priority landing
86 sites and enable them to directly probe the methane source. The results can also guide orbiting
87 instruments to better focus their methane observation strategies.

88 Inferring the locations of methane emission sites requires correct modeling of complex
89 atmospheric transport processes. An early attempt to do so involved using a diffusion model to
90 represent the spread of observed methane plumes (Mumma et al., 2009), which was shown to be
91 oversimplified by addressing the importance of advection by bulk wind (Mischna et al., 2011).
92 More recently, the Global Environmental Multiscale (GEM)-Mars general circulation model
93 (GCM) was used to simulate methane transport and then a statistical approach based on the idea
94 of simultaneous satisfaction of multiple observational constraints was used for methane source
95 localization (Giuranna et al., 2019). Results suggested an emission region to the east of Gale
96 crater for TLS's first methane spike (Spike 1 in Fig. 1). Later, the Mars Regional Atmospheric
97 Modeling System (MRAMS) model was used to simulate the transport and dispersion of
98 methane plumes emitted from ten selected source regions around Gale crater (Pla-García et al.,
99 2019). Substantial dilution during tracer transport was observed, which demonstrates the
100 importance of incorporating turbulent dispersion into tracer transport modeling. Among all the

ten emission region candidates, the region to the northwest of the crater was favored, different from previous findings (e.g., Giuranna et al., 2019).

The aforementioned emission site localization studies all adopted a forward Eulerian approach, in which the model integrates three-dimensional tracer fields forward in time and quantifies how much tracer released at a specific emission location and time can ultimately reach the detector. However, this "trial-and-error" approach is computationally inefficient, as most of the released particles do not reach the detector, so usually only a small number of putative emission sites are selected and studied in depth (e.g., Pla-García et al., 2019). Meanwhile, the spatial resolution of emission regions is limited by the size of GCM grid boxes, making it difficult to differentiate emission sites within Gale crater (e.g., Giuranna et al., 2019).

In this work, we adopt an inverse Lagrangian approach (Lin et al., 2003, 2012) to overcome the challenges faced by forward Eulerian emission site localization techniques. The inverse Lagrangian approach is also known as back-trajectory analysis and is widely used in the environmental science community to map out upstream emission regions (e.g., Lin et al., 2003; Gerbig et al., 2003; Lin et al., 2004; Kort et al., 2008; Macatangay et al., 2008; Mallia et al., 2015). An ensemble of computational particles, representing air parcels, is released from the detector at the time of detection and is transported backwards in time. The particles' transport pathways are determined by the bulk wind, and the particles are dispersed by parameterized subgrid-scale turbulence. The locations where backward-travelling particles are found within the PBL and hence are potentially affected by surface emission are identified as potential upstream emission regions. The quantitative linkage between measured atmospheric mole fraction at the detector and upstream surface fluxes is established via the number density of particles at an upstream location (Lin et al., 2003; Fasoli et al., 2018). A single inverse Lagrangian simulation

can quantify the influence of all upstream emission regions on a detection, and the spatial resolution of emission regions is not limited by the GCM resolution. As such, high-resolution maps of all upstream emission regions can be produced, which is critical for the search for emission sites within and around the small, 154-km wide, Gale crater.

2 Methods

2.1 GCM wind simulations

Since global, high-quality wind observations on Mars have been lacking to date, we use MarsWRF, a GCM of the Martian atmosphere, to simulate the wind fields necessary for inverse Lagrangian modeling. MarsWRF is derived from the terrestrial WRF model and is a Mars-specific implementation of PlanetWRF (Christensen et al., 2001). MarsWRF is a finite-difference grid-point model projected onto an Arakawa-C grid with user-defined horizontal and vertical resolutions. The vertical grid follows a modified-sigma (terrain-following) coordinate from the surface to ~80 km altitude. The total present-day atmospheric CO_2 budget is tuned to fit the Viking Lander annual pressure curves (~6.1 mbar), and both surface albedo and thermal inertia are matched to Mars Global Surveyor Thermal Emission Spectrometer (MGS-TES) observations (Christensen et al., 2001; Putzig et al., 2005), while a Mars Orbiter Laser Altimeter (MOLA) topography base map is employed and scaled to the chosen model resolution.

Multiple studies in the past have validated MarsWRF to the maximum possible extent through comparison of its behavior against data from the *Mars Global Surveyor* Thermal Emission Spectrometer (Lee et al., 2011; Toigo et al., 2012; Guzewich et al., 2013, 2014), the *Mars Reconnaissance Orbiter* Mars Climate Sounder (Guzewich et al.,

2013), and the weather stations on board *Curiosity* (Fonseca et al., 2018; Newman et al., 2017) and *InSight* (Newman et al., 2020), showing MarsWRF reproduces observed atmospheric pressure, atmospheric and ground temperature, near-surface wind speeds and wind directions reasonably well.

MarsWRF permits multiple embedded "nests" with increasing spatial resolutions in a single model run. This allows atmospheric circulations influenced by small-scale topographic features to be fully resolved in a simulation while the simulation also covers the entire globe. In this study, we run MarsWRF at increasing horizontal resolutions around Gale crater. The final model consists of four nested levels, each scaled up in resolution (spatial and temporal) by a factor of three. Level 1 provides global coverage with a horizontal resolution of 2°×2° and a 60-second timestep. Level 2 encompasses an 80°×80° domain with a horizontal resolution of 0.67°×0.67° and a 20-second timestep. Level 3 encompasses a 26.67°×26.67° domain with a horizontal resolution of 0.222°×0.222° and a 6.67-second timestep. Level 4 encompasses an 8.89°×8.89° domain with a horizontal resolution of 0.074°×0.074° (4.4 km×4.4 km) and a 2.22-second timestep (Fig. S1), which fully resolves the crater circulation. Two-way boundary conditions link a nested domain with its "parent", with information being passed both up and down between parent and child domains. A description of this process may be found in Richardson et al. (2007). In order to speed up the simulations, we performed test simulations in advance to determine the duration of MarsWRF simulations on each

nesting level. A higher-level nesting is no longer necessary after 99% of the initially released backward-traveling particles have left the domain of that nesting level.

Given the lack of a global coverage of high-quality wind observations, it is impossible to reproduce precise "real" atmospheric circulations on spatial scales smaller than tens of kilometers, as stochastic weather events can significantly impact wind speed and even direction. As a result, at this stage, we do not intend to reproduce the "real" winds. Instead, we aim to produce "mean" winds that are representative of their respective seasons and time of day. For each TLS measurement, we repeat MarsWRF simulations for the corresponding Mars year five times, each time starting from a different initial condition. For each Mars year, the different rounds of GCM simulations are all driven by the same seasonally representative dust loadings. They show slight variations in year-to-year conditions as a consequence of stochastic variability in the weather. The variance in results across the five times of simulation is, however, small.

On short timescales (<1 week), it is not anticipated there will be a significant change in the mean atmospheric conditions on Mars, so for each of the five rounds of wind simulations, we treat the sol of measurement, and one, two, three sols before and after the measurement as equally representative of the circulation pattern at the time of the TLS measurement, and release particles at the time of day of each measurement on all of the seven sols. In this way, we form an ensemble of thirty-five back-trajectory simulations for each investigated TLS measurement, and the following analysis is all

186 based on the average footprints of these thirty-five simulations. This ensures that discrete
187 weather patterns are smoothed out.

188 2.2 Inverse Lagrangian analysis

189 The wind fields from MarsWRF are used to drive the Stochastic Time-Inverted
190 Lagrangian Transport (STILT) Lagrangian Particle Dispersion Model (Lin et al., 2003;
191 Fasoli et al., 2018) to simulate plume transport and dispersion. STILT is based on the
192 Hybrid Single Particle Lagrangian Integrated Trajectory (HYSPLIT) model (Draxler and
193 Hess, 1998; Stein et al., 2015) that is extensively used in air quality, volcanic ash and
194 industrial plume modeling, and STILT inherits all of the validated components of its
195 predecessor. In its application, STILT transports an ensemble of computational particles
196 (ten thousand particles in each simulation in this study) from the site of the detector (here,
197 the location of the *Curiosity* rover) using time-reversed grid-scale wind plus a
198 parameterized subgrid-scale turbulent velocity (Hanna, 1984). The timestep in STILT is
199 determined dynamically based on the wind field, and typically ranges between one
200 minute and ten minutes. When combined with a GCM, STILT linearly interpolates the
201 simulated bulk wind from the GCM grid points to the precise positions of each particle at
202 each timestep, and then displaces the particles according to the reversed wind arrow.
203 Meanwhile, STILT adds a random velocity component, determined by a Markov chain
204 process based statistically on the simulated meteorological conditions, to the bulk wind
205 velocity. The random velocity represents turbulent motions that are unresolved by the
206 GCM and results in dispersion of the particle cloud (Fig. S3). Additionally, vertical
207 mixing in the PBL is parameterized by vertically redistributing particles to random
208 altitudes within the PBL (Fig. S4). In the hyper-near field around the detector, an

209 "effective mixing depth" smaller than the PBL thickness is calculated based on the
210 homogeneous turbulence theory (Fasoli et al., 2018). This will prevent the particles
211 released near the surface from ascending to the top of the PBL instantaneously.

212 At every timestep in a back-trajectory simulation (which corresponds to an
213 emission time), STILT tallies the instantaneous particle density in the PBL at all locations
214 and generates a "footprint" map in units of ppbv μmol^{-1} (Lin et al., 2003), which
215 quantifies the contribution of unit methane emission flux from an emission site to the
216 methane mole fraction at the detector. The STILT footprint is proportional to the column-
217 integrated particle number density within the PBL and the molar mass of air, and
218 inversely proportional to the PBL thickness and the average air density within the PBL
219 (Lin et al., 2003). The value of the footprint at an emission site is equal to the prospected
220 methane mole fraction in the unit of ppbv above the ~0.41 ppbv background level
221 induced by 1 μmol of methane emission at that emission site. High footprints indicate
222 regions where the emission casts strong influence over the detection, or in brief, the
223 upstream regions. Since the circulation pattern changes all the time, the footprint values
224 at the same emission site at different emission times are also different. If integrated over a
225 certain period of emission time, the footprints will measure the influence of a constant-
226 flux emission in that period of emission time on a detection, and the pattern of the time-
227 integrated footprints will show all upstream regions.

228 In computing the footprints, the domain is first gridded horizontally (a grid that is
229 separate from that of the GCM) so that STILT can count the number of particles within
230 each horizontal grid and calculate the particle density at all horizontal locations. The
231 resolution of this grid becomes the resolution of the footprints, and hence the resolution

of the emission regions. We use 2° as the resolution for the domain from 80°S to 80°N and from 60°E eastward to 140°W. For the subdomain from 17.6°S to 8.4°N, from 124.2°E to 150.4°E, we use a higher resolution of 0.2°, or ~11.8 km. For the subdomain from 6.64°S to 3.72°S, from 136.24°E to 139.16°E, we use a further higher resolution of 0.02°, or ~1.18 km. We note that the definition of the STILT footprint in this study is slightly different from that in Lin et al. (2003). The new definition has excluded the influence of the grid size and the timestep of the footprint calculation on the values of the footprints.

STILT was originally designed for terrestrial use, and we adapted STILT so that it can be used for Mars. The modifications include changes to planetary radius, gas constant, angular rotation rate of the planet, surface gravity, dynamic viscosity of air, mean free path of air, molecular weight of air, surface air pressure, specific heat capacity of air, the map of land use, and the map of surface roughness length (Hébrard et al., 2012), etc. We note that the Monin–Obukhov similarity theory for the PBL, along with the adherence to the well-mixed criterion (Thomson, 1987), a manifestation of the second law of thermodynamics, ensures that the physics and fluid dynamics underlying STILT can be applied to all substantial planetary atmospheres, including the Martian atmosphere.

3 Results

3.1 Categorization of methane spikes

We focus on the six methane spikes reported by the TLS instrument (which is referred to as the “detector” in the following text) during the 4.6 years of the *Curiosity*

mission through May 2017 (Fig. 1, Table S1). The six spikes can be categorized based on the seasons and the time of day of their detections. In terms of seasons, Spikes 1 and 6 were detected from late northern fall into winter. Spikes 2–5 were detected in northern spring. In terms of the time of day, Spikes 1 and 5 were detected in the early afternoon, and Spikes 2, 3, 4 and 6 were detected between midnight and early morning. As a result, Spikes 1 and 6 share similar seasonal, regional and global circulation patterns, as do Spikes 2–5. Spikes 1 and 5 share similar diurnal crater circulation patterns, as do Spikes 2, 3, 4 and 6. The similarity in atmospheric circulation patterns also manifests itself in the subsequent STILT footprint maps.

3.2 Atmospheric circulations

MarsWRF simulations show that the circulation at Gale crater consists of three components – a global meridional overturning circulation, a regional circulation, and a crater-scale circulation. Figure 2 shows an example of near-surface winds simulated by MarsWRF. In northern winter, the rising branch of the global meridional overturning circulation is centered in the southern hemisphere. Prevailing winds at the topographic dichotomy next to Gale crater are southward and are particularly strong around 270° solar longitude when Spike 6 was detected. In northern spring, the large-scale prevailing winds at Gale crater are weak. The regional circulation is characterized by upslope northerlies along the topographic dichotomy in the afternoon, and downslope southerlies in the nighttime. The crater circulation is characterized by upslope winds along the inner crater rim and the slope of Mount Sharp in the afternoon, and downslope winds in the nighttime. The PBL thickness at Gale crater undergoes a daily cycle between a nighttime

minimum thickness of tens of meters, and a daytime maximum thickness of about three kilometers, similar to previous findings in Fonseca et al. (2018).

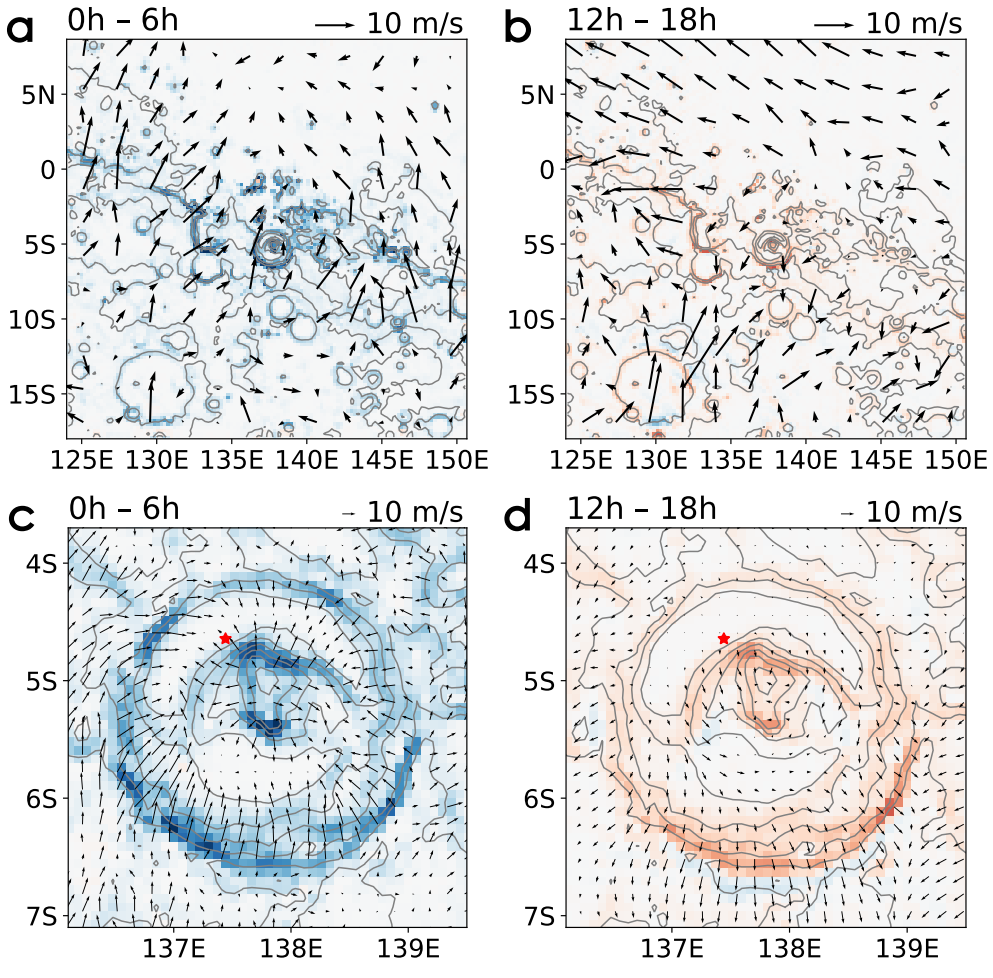

Figure 2. Simulated winds in the bottom layer of MarsWRF at 81.84° solar longitude (concurrent with Spike 5). The plotted data is an average over six hours as indicated by the time period on the upper left of each panel. (**a**) and (**b**) show the regional circulation, from which one can identify southwesterly downslope winds along the topographic dichotomy from midnight to sunrise, and northeasterly upslope winds from noon to sunset. (**c**) and (**d**) show the Gale crater circulation, from which one can identify downslope winds along the inner wall of the crater rim and along Mount Sharp from midnight to sunrise, and upslope winds from noon to

sunset. The crater circulation is well resolved by MarsWRF. Red colors show rising air. Blue colors show sinking air. Contours show surface elevation. Red stars mark the position of *Curiosity*.

3.3 Identifying upstream regions

Figure 3 shows the time-integrated footprints for Spikes 1 and 2. Refer to Fig. 5 and Fig. S5 for the footprints for Spikes 3–6. Within Gale crater, the strongest footprint of Spike 1 lies to the north of the TLS detector (Fig. 3a), which is also the case for Spike 5 (Fig. S5g). This means that these two early-afternoon measurements are both more sensitive to the emission from the north compared to the emission from other directions. The similarity in the footprints for Spikes 1 and 5 is consistent with the similarity in the early-afternoon crater-scale circulation patterns at the *Curiosity* site, in which northerlies dominate, although Spikes 1 and 5 were detected in different seasons. For Spike 2, the strongest footprint lies on the entire northwestern crater floor (Fig. 3d). This is also the case for Spikes 3, 4, and 6 (Fig. 5d, Fig. S5a, d), although there are some finer spatial patterns in the footprints for Spike 6. These four spikes were all detected in the nighttime when the PBL was shallow. The released particles are confined within the PBL and therefore imprint almost equally strong footprints onto the entire northwestern crater

floor as they are transported backwards in time. In other words, a nighttime detection is sensitive to the emission from any place on the northwestern crater floor.

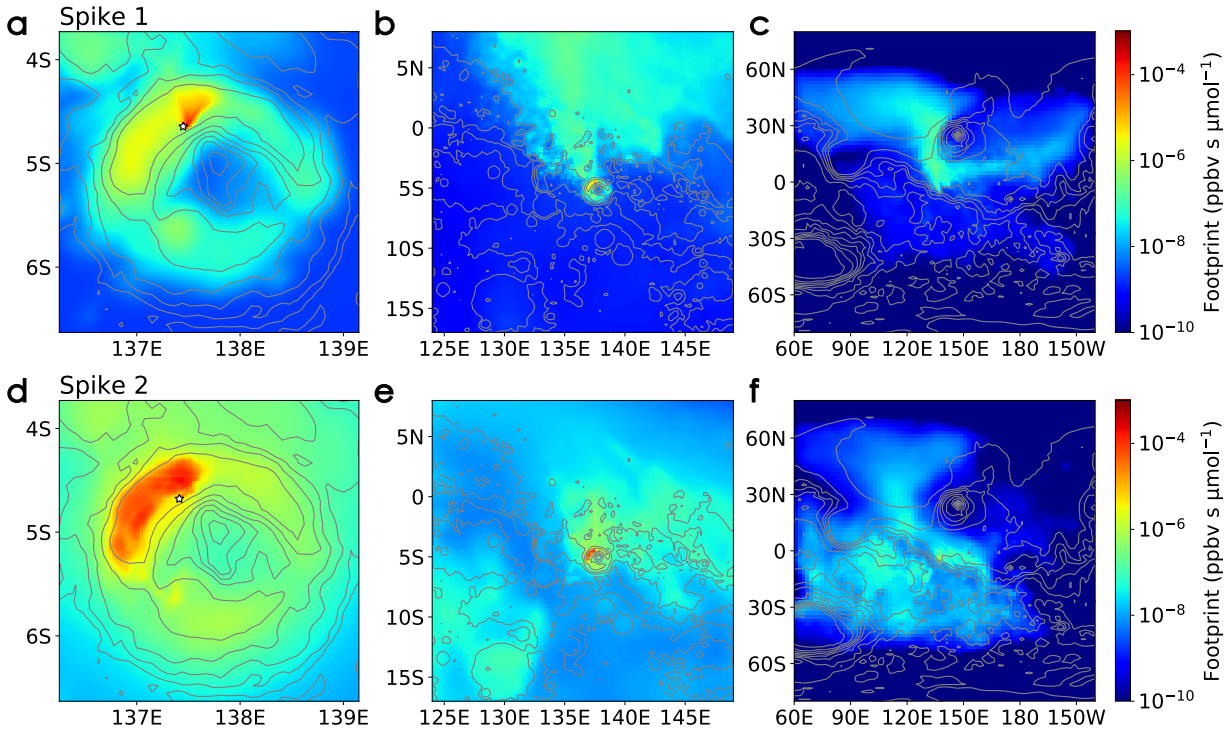

Figure 3. Influence of emission fluxes at any emission site on (a–c) Spike 1 and (d–f) Spike 2, shown in (a, d) the crater scale, (b, e) the regional scale, and (c, f) the hemispherical scale. Colors show STILT footprints integrated backwards in time over thirty sols. High values of footprints indicate upstream regions. The values of the footprints are equal to the prospected TLS methane signals in ppbv above the ~0.41 ppbv background after a thirty-sol constant-flux methane emission event with an emission flux of 1 µmol s^{-1} occurs at one emission site. Stars in (**a**) and (**d**) mark the positions of *Curiosity*.

Outside Gale crater, the strongest footprint for Spike 1 lies to the north of the crater, as a result of the prevailing regional-scale northerlies in this season (Fig. 3b). This is also true for Spike 6 (Fig. 5e). This shows that for these two spikes, if a methane

316 emission region exists in the neighborhood of Gale crater (but outside the crater), it is
317 most likely located to the north of the crater. The locations of the upstream regions for
318 Spike 2 are, however, less definitive. The strongest footprints for Spike 2 cover the
319 regions in the first and third quadrants of Gale crater (Fig. 3e). This is also the case for
320 Spikes 3–5 (Fig. S5b, e, h). Despite this ambiguity, the strongest footprints for all the six
321 spikes overlap in a region within 300 km to the north of Gale crater. It is noteworthy that
322 the "E8" and "ESE" regions, suggested as the most likely emission regions for Spike 1
323 (Giuranna et al., 2019), do not bear strong footprints in our study and are hence not
324 identified as the preferred upstream regions for Spike 1 (Fig. 3b).

325 Further zooming out to the hemispherical scale, the strongest footprints for Spike
326 1 extend from Elysium Planitia towards two directions – one heading for the north along
327 the western side of Elysium Mons to Utopia Planitia, and the other heading for the east
328 along the southern side of Elysium Mons to Amazonis Planitia (Fig. 3c). This is also the
329 case for Spike 6, although the northern branch appears more prominent (Fig. 5f). This
330 suggests that the aforementioned large-scale geographic units are more likely to be the
331 emission regions than other large-scale geographic units for Spikes 1 and 6. For Spikes
332 2–5, the strong footprints cover many large-scale geographic units around Gale crater
333 (Fig. 3f, Fig. S5c, f, i), including the aforementioned Elysium Planitia and Utopia
334 Planitia.

335 3.4 Minimum methane emission

336 Based on the footprints, the minimum amount of methane emitted from any
337 emission site that could give rise to the observed methane spikes can be calculated. TLS's

338 ~0.41 ppbv background level is first subtracted from the six methane spikes. The
339 remainder of the signals must then be a consequence of recent emission. It is unknown
340 whether the emission was continuous, intermittent, or episodic, but to put a lower bound
341 on the required methane emission, we can assume the emission was instantaneous and
342 occurred at the exact moment when an emission site had the strongest influence on a
343 detection. Then, dividing each methane signal (with the background signal subtracted) by
344 the maximum footprint at an emission site yields the minimum amount of methane
345 emitted from that emission site required by the methane signal (Fig. 4). Upstream
346 regions, which show up with the highest footprint values in Fig. 3, now bear the smallest
347 values in Fig. 4, the latter meaning that they can more easily produce a methane signal.
348 For example, the northwestern crater floor (the blue region in Fig. 4d) is able to produce
349 Spike 2 by emitting only about a hundred kilograms of methane, which will result in an
350 increase of ~10^{-5} ppbv in the global mean methane concentration, assuming the emission
351 occurred at the exact moment when it cast the highest influence over the detection. In
352 contrast, if Spike 2 results from an emission event in Utopia Planitia, at least several
353 millions of kilograms of methane must have been emitted, which will result in an

increase of several hundreds of pptv (parts-per-trillion-by-volume, 1 pptv = 10^{-3} ppbv) in the global mean methane concentration (Fig. 4f).

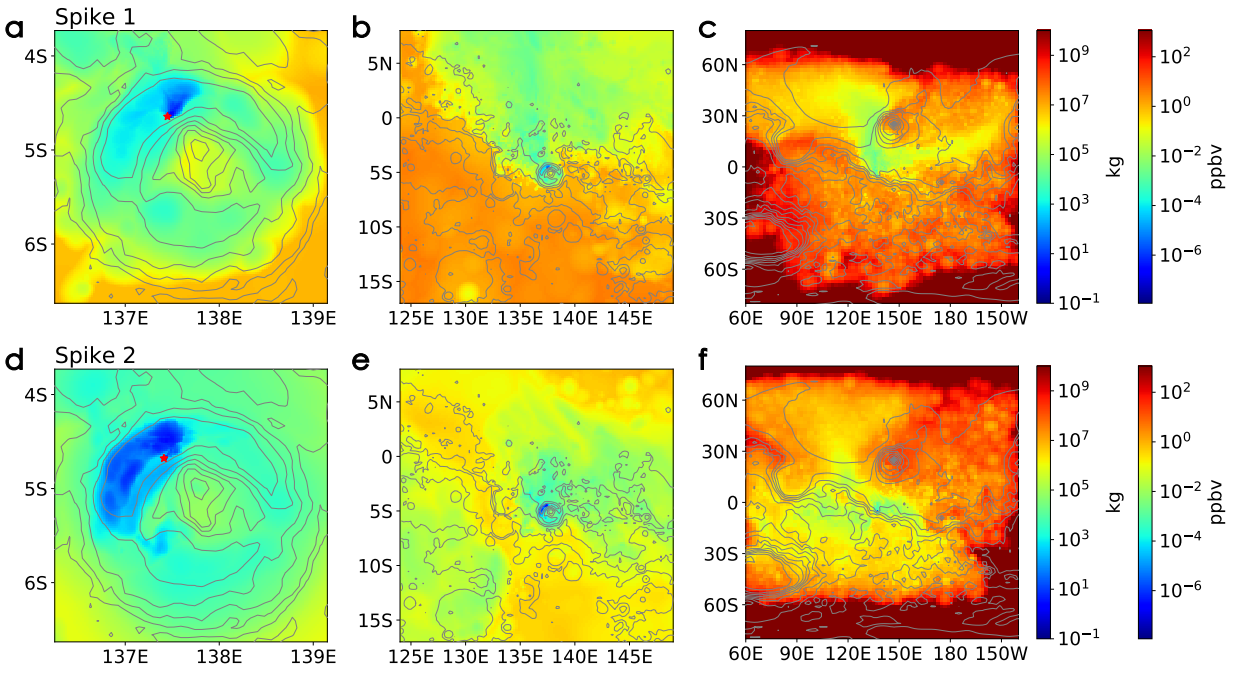

Figure 4. The minimum amount of methane emitted from different locations that can produce (a–c) Spike 1 and (d–f) Spike 2. The emission is assumed to occur at the moment when an emission site has the strongest influence on a detection. The left colorbars show the minimum mass of emitted methane as required by the magnitude of the spikes. The right colorbars show the increase in the globally averaged methane concentration after an aforementioned smallest emission event occurs. Stars in (**a**) and (**d**) mark the positions of *Curiosity*.

TGO's 0.02 ppbv upper limit (Montmessin et al., 2021), interpreted as the upper limit on the average methane concentration in the Martian atmosphere, if combined with the 330-year lifetime from standard photochemical models (Lefèvre and Forget, 2009), implies that on average no more than 6×10^{-5} ppbv of methane (or ~520 kg of methane) is

368 replenished every year. Then, during the 4.6 years of TLS operation, on average, no more
369 than ~2.8×10^{-4} ppbv (or ~2400 kilograms) was emitted into the atmosphere. Assuming
370 the six methane spikes result from six emission events, on average, each of them can emit
371 no more than ~400 kilograms of methane; otherwise, they would have resulted in a
372 significant and potentially observable rise in the background methane concentration.
373 Only the blue areas in Fig. 4 are such qualified areas that are able to produce a methane
374 spike with the observed mole fraction by emitting 400 kilograms of methane. More
375 quantitative analysis shows that the "qualified areas" are only 1300 km^2 in total, about
376 7% the total area of Gale crater (Fig. S10). This means that without fast removal
377 mechanisms that can significantly reduce the methane lifetime, the methane emission site
378 that is responsible for the TLS methane spikes has to be located within the 1300 km^2
379 around the *Curiosity* site inside Gale crater, and no other emission sites can exist over the
380 planet. This is the only way that the TLS spikes and the TGO non-detections can be
381 reconciled. The 1300 km^2 area is probably still an overestimate, as the assumed situation
382 where only six methane emission events occurred during the 4.6 years and all of them
383 were captured by the TLS measurements is almost impossible. The actual methane spike
384 frequency at the *Curiosity* site may be much higher, which will put a much lower upper
385 bound on the amount of methane emitted by a single emission event. In that case, the
386 qualified emission regions will be confined within even smaller areas that are very close
387 to the location of the *Curiosity* rover, such as the deep blue areas on the northwestern
388 crater floor in Fig. 4. Even the 1300 km^2 upper limit of the qualified emission region will
389 invoke an coincidence that *Curiosity* was sent to the vicinity of the only methane
390 emission hotspot on Mars. One possibility that does not invoke the coincidence is that

391 unknown, rapid methane removal mechanisms are at work. If the methane lifetime is
392 shorter than 330 years, more methane can be emitted into the atmosphere per year
393 without perturbing the long-term background methane concentration, and the emission
394 sites will have some freedom to be located at distant places outside Gale crater, most
395 likely in the upstream regions found in Section 3.3. Refer to Fig. S10 for a more
396 quantitative analysis on the required "coincidence" if we accept the results from both
397 TLS and TGO and the 330-year methane lifetime from classical models. To summarize,
398 under the three assumptions – 1. TLS's methane spikes are real, 2. TGO's upper limits
399 are real and they represent the upper limit of the methane abundance throughout the
400 Martian atmosphere, and 3. the methane lifetime is ~330 years – there will be only one
401 methane emission region over the entire globe, and it is within an area of 1300 km^2
402 around the *Curiosity* site in northwestern Gale crater. This may just be a coincidence, as
403 Gale crater was carefully selected as the landing site for the *Curiosity* rover based on its
404 unique geological context (e.g., Grotzinger et al., 2015). Otherwise, at least one of the
405 three assumptions above needs to be reevaluated.

406 3.5 Consecutive methane measurements

407 More precise emission site identification is possible when we make use of
408 consecutive methane measurements that reported a large difference in methane
409 abundances. At ~266° solar longitude in Mars Year 33, two measurements were
410 consecutively performed within a few hours. The first measurement started at ~01:30
411 local time and detected a 0.332 ppbv signal, close to the background level. Only a few
412 hours later, the second measurement at ~06:30 local time detected Spike 6 with 5.55
413 ppbv. One possible explanation for the rapid increase in the ambient methane

414 concentration is the initiation of an emission event between the two measurements. Here,
415 we focus on another possibility that a change in wind directions between the two
416 measurements induced the temporal variability of the methane signals. If an emission
417 event occurred before the two methane measurements, it would produce a methane signal
418 only if the emission site was located in the upstream region of the detector at the time of
419 emission. Figure 5 shows a comparison between the time-integrated footprints for Spike
420 6 and those for the background level. A significant difference can be found between the
421 upstream regions within Gale crater (Fig. 5a, d). On the northwestern crater floor, the
422 upstream region of Spike 6, indicated by high footprint values, primarily lies to the west
423 and the southwest of *Curiosity* rover, whereas the upstream region of the background
424 level primarily lies to the northeast of the rover. Therefore, the region to the west and the
425 southwest of *Curiosity* in northwestern Gale crater is identified as a highly probable

location of an emission site. There are not significant differences between the upstream regions at larger scales (Fig. 5b, e, and Fig. 5c, f).

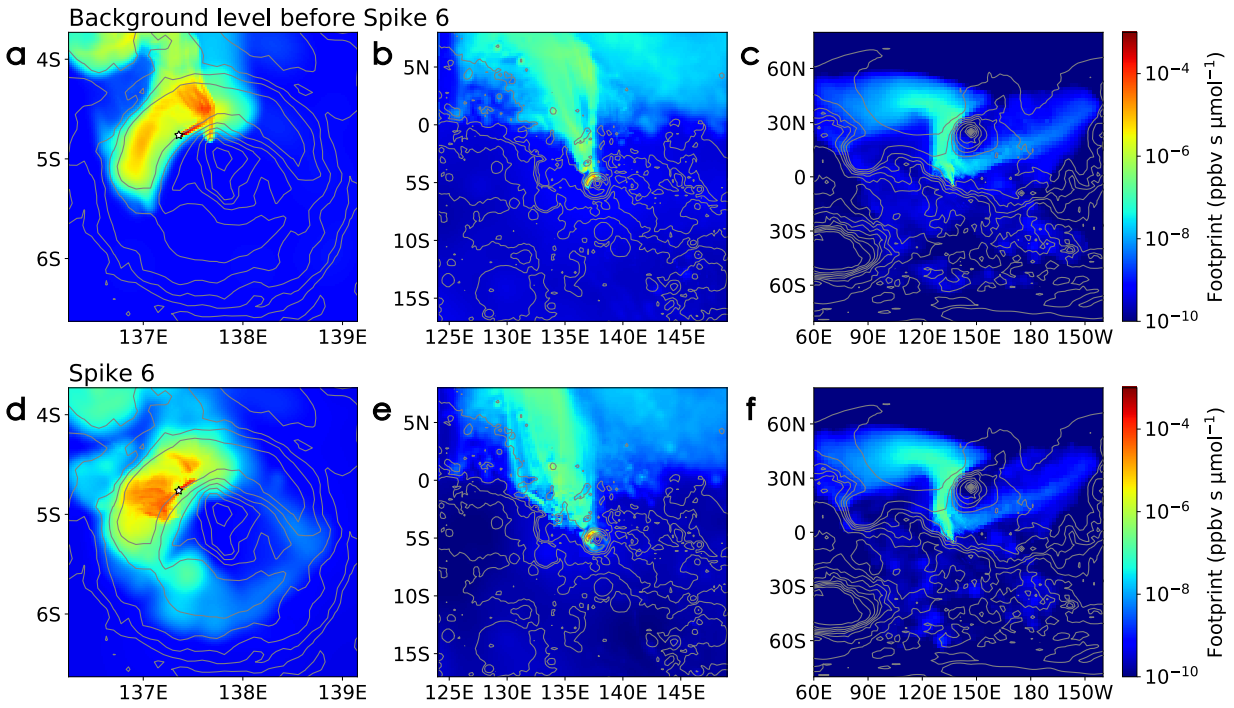

Figure 5. Comparison of the footprints for the background level and for Spike 6, both measured at ~266° solar longitude in Mars Year 33. Panels (**a**–**c**) show the STILT footprint for the background concentration. (**d**–**f**) show the STILT footprint for Spike 6. The stars in (**a**) and (**d**) show the positions of *Curiosity*. An emission site with weak influence on the background level and strong influence on Spike 6 will be bearing a small footprint for the former and a large footprint for the latter. Comparing (**a**) and (**d**), regions to the west and the southwest of *Curiosity* on the northwestern crater floor are such regions. The differences between (**b**) and (**e**) and between (**c**) and (**f**) at the larger scales are not significant.

We note that this method based on consecutive methane measurements is able to precisely constrain the location of a nearby emission site, but it requires consecutive

measurements performed within a short period of time, shorter than a few days and optimally a few hours. Fortunately, the measurement strategy of TLS, which often performs paired measurements within a few hours, meets this requirement.

4 Conclusions

In conclusion, if we trust the methane abundances detected by both TLS and TGO and accept the 330-year methane lifetime from known photochemistry, our back-trajectory modeling for atmospheric transport strongly supports surface emission sites in the vicinity of the *Curiosity* rover in northwestern Gale crater. This may invoke a coincidence that we selected a landing site for *Curiosity* that is located next to an active methane emission site. Other possibilities that does not invoke the coincidence include the existence of fast methane removal mechanisms that are unknown to date, and false positives of TLS and false negatives of TGO. Should future studies confirm the existence of heterogeneous pathways or other unknown photochemical processes for methane destruction, the methane emission sites can be located outside Gale crater, and most likely to the north of the crater. Continuing the TLS and the TGO measurements of methane concentration at Gale crater still seems to be the best move for now.

Our study demonstrates the feasibility and the advantages of applying the inverse Lagrangian modeling technique to source localization problems on other planets. Methane abundance data from future in situ measurements, especially those collected in consecutive measurements performed within a few hours, would further improve the source localization.

Acknowledgments, Samples, and Data

A portion of this research was carried out at the Jet Propulsion Laboratory, California Institute of Technology, under contract with NASA. Government sponsorship acknowledged. Y. L. Y

acknowledges the President's and Director's Research and Development Fund and the support from the Virtual Planetary Laboratory at the University of Washington that is funded via NASA Astrobiology Program Grant No. 80NSSC18K0829. Resources supporting this work were provided by the NASA High-End Computing (HEC) Program through the NASA Advanced Supercomputing (NAS) Division at Ames Research Center.

A file that lists all the relevant conditions and parameters used in the MarsWRF simulations can be found at the CaltechDATA reposity via https://doi.org/10.22002/D1.2026. The original STILT model is available at its website https://uataq.github.io/stilt/#/. A list of modifications to the original STILT model based on the conditions of Mars can be found at the CaltechDATA repository via https://doi.org/10.22002/D1.2026. The STILT footprint files used to generate Figure 3–5 in this study are available at the CaltechDATA repository via https://doi.org/10.22002/D1.2025.

References

1. Aoki, S., Richter, M. J., DeWitt, C., Boogert, A., Encrenaz, T., Sagawa, H., et al. (2018). Stringent upper limit of CH_4 on Mars based on SOFIA/EXES observations. *Astronomy & Astrophysics*, *610*, A78. https://doi.org/10.1051/0004-6361/201730903
2. Christensen, P. R., Bandfield, J. L., Hamilton, V. E., Ruff, S. W., Kieffer, H. H., Titus, T. N., et al. (2001). Mars Global Surveyor Thermal Emission Spectrometer experiment: investigation description and surface science results. *Journal of Geophysical Research: Planets*, 106(E10), 23823-23871. https://doi.org/10.1029/2000JE001370
3. Cicerone, R. J., & Oremland, R. S. (1988). Biogeochemical aspects of atmospheric methane. *Global Biogeochemical Cycles*, *2*(4), 299-327. https://doi.org/10.1029/GB002i004p00299
4. Draxler, R. R., & Hess, G. D. (1998). An overview of the HYSPLIT_4 modelling system for

trajectories. *Australian Meteorological Magazine*, 47(4), 295-308.

5. Fasoli, B., Lin, J. C., Bowling, D. R., Mitchell, L., & Mendoza, D. (2018). Simulating atmospheric tracer concentrations for spatially distributed receptors: updates to the Stochastic Time-Inverted Lagrangian Transport model's R interface (STILT-R version 2). *Geoscientific Model Development*, 11(7), 2813-2824. https://doi.org/10.5194/gmd-11-2813-2018
6. Fonseca, R. M., Zorzano-Mier, M. P., & Martín-Torres, J. (2018). Planetary boundary layer and circulation dynamics at Gale Crater, Mars. *Icarus*, 302, 537-559. https://doi.org/10.1016/j.icarus.2017.11.036
7. Fonti, S., & Marzo, G. A. (2010). Mapping the methane on Mars. *Astronomy & Astrophysics*, *512*, A51. https://doi.org/10.1051/0004-6361/200913178
8. Formisano, V., Atreya, S., Encrenaz, T., Ignatiev, N., & Giuranna, M. (2004). Detection of methane in the atmosphere of Mars. *Science*, *306*(5702), 1758-1761. https://doi.org/10.1126/science.1101732
9. Geminale, A., Formisano, V., & Giuranna, M. (2008). Methane in Martian atmosphere: average spatial, diurnal, and seasonal behaviour. *Planetary and Space Science*, *56*(9), 1194-1203. https://doi.org/10.1016/j.pss.2008.03.004
10. Gerbig, C., Lin, J. C., Wofsy, S. C., Daube, B. C., Andrews, A. E., Stephens, B. B., et al. (2003). Toward constraining regional-scale fluxes of CO_2 with atmospheric observations over a continent: 2. Analysis of COBRA data using a receptor-oriented framework. *Journal of Geophysical Research: Atmospheres*, 108(D24). https://doi.org/10.1029/2003JD003770
11. Giuranna, M., Viscardy, S., Daerden, F., Neary, L., Etiope, G., Oehler, D., et al. (2019). Independent confirmation of a methane spike on Mars and a source region east of Gale Crater. *Nature Geoscience*, *12*(5), 326-332. https://doi.org/10.1038/s41561-019-0331-9

12. Gough, R. V., Tolbert, M. A., McKay, C. P., & Toon, O. B. (2010). Methane adsorption on a Martian soil analog: An abiogenic explanation for methane variability in the Martian atmosphere. *Icarus*, 207(1), 165-174. https://doi.org/10.1016/j.icarus.2009.11.030
13. Grotzinger, J. P., Gupta, S., Malin, M. C., Rubin, D. M., Schieber, J., Siebach, K., et al. (2015). Deposition, exhumation, and paleoclimate of an ancient lake deposit, Gale crater, Mars. *Science*, 350(6257). https://doi.org/10.1126/science.aac7575
14. Guzewich, S. D., Talaat, E. R., Toigo, A. D., Waugh, D. W., & McConnochie, T. H. (2013). High-altitude dust layers on Mars: Observations with the Thermal Emission Spectrometer. *Journal of Geophysical Research: Planets*, 118(6), 1177-1194. https://doi.org/10.1002/jgre.20076
15. Guzewich, S. D., Wilson, R. J., McConnochie, T. H., Toigo, A. D., Banfield, D. J., & Smith, M. D. (2014). Thermal tides during the 2001 Martian global-scale dust storm. *Journal of Geophysical Research: Planets*, 119(3), 506-519. https://doi.org/10.1002/2013JE004502
16. Hanna, S. R. (1984). Applications in air pollution modeling. In Atmospheric turbulence and air pollution modelling (pp. 275-310). Springer, Dordrecht. https://doi.org/10.1007/978-94-010-9112-1_7
17. Hébrard, E., Listowski, C., Coll, P., Marticorena, B., Bergametti, G., Määttänen, A., et al. (2012). An aerodynamic roughness length map derived from extended Martian rock abundance data. *Journal of Geophysical Research: Planets*, 117(E4). https://doi.org/10.1029/2011JE003942
18. Hu, R., Bloom, A. A., Gao, P., Miller, C. E., & Yung, Y. L. (2016). Hypotheses for near-surface exchange of methane on Mars. *Astrobiology*, 16(7), 539-550. https://doi.org/10.1089/ast.2015.1410

19. Kite, E. S., Gao, P., Goldblatt, C., Mischna, M. A., Mayer, D. P., & Yung, Y. L. (2017). Methane bursts as a trigger for intermittent lake-forming climates on post-Noachian Mars. *Nature Geoscience*, *10*(10), 737-740. https://doi.org/10.1038/ngeo3033

20. Knak Jensen, S. J., Skibsted, J., Jakobsen, H. J., Inge, L., Gunnlaugsson, H. P., Merrison, J. P., et al. (2014). A sink for methane on Mars? The answer is blowing in the wind. *Icarus*, 236, 24-27. https://doi.org/10.1016/j.icarus.2014.03.036

21. Knutsen, E. W., Villanueva, G. L., Liuzzi, G., Crismani, M. M., Mumma, M. J., Smith, M. D., et al. (2021). Comprehensive investigation of Mars methane and organics with ExoMars/NOMAD. *Icarus*, 357, 114266. https://doi.org/10.1016/j.icarus.2020.114266

22. Korablev, O., Vandaele, A. C., Montmessin, F., Fedorova, A. A., Trokhimovskiy, A., Forget, F., et al. (2019). No detection of methane on Mars from early ExoMars Trace Gas Orbiter observations. *Nature*, 568(7753), 517-520. https://doi.org/10.1038/s41586-019-1096-4

23. Kort, E. A., Eluszkiewicz, J., Stephens, B. B., Miller, J. B., Gerbig, C., Nehrkorn, T., et al. (2008). Emissions of CH_4 and N_2O over the United States and Canada based on a receptor-oriented modeling framework and COBRA-NA atmospheric observations. *Geophysical Research Letters*, 35(18). https://doi.org/10.1029/2008GL034031

24. Krasnopolsky, V. A. (2012). Search for methane and upper limits to ethane and SO2 on Mars. *Icarus*, *217*(1), 144-152. https://doi.org/10.1016/j.icarus.2011.10.019

25. Krasnopolsky, V. A., Maillard, J. P., & Owen, T. C. (2004). Detection of methane in the martian atmosphere: evidence for life?. *Icarus*, *172*(2), 537-547. https://doi.org/10.1016/j.icarus.2004.07.004

26. Lee, C., Lawson, W. G., Richardson, M. I., Anderson, J. L., Collins, N., Hoar, T., & Mischna, M. (2011). Demonstration of ensemble data assimilation for Mars using DART,

553 MarsWRF, and radiance observations from MGS TES. *Journal of Geophysical Research:*
554 *Planets*, 116(E11). https://doi.org/10.1029/2011JE003815
555 27. Lefèvre, F., & Forget, F. (2009). Observed variations of methane on Mars unexplained by
556 known atmospheric chemistry and physics. *Nature*, 460(7256), 720-723.
557 https://doi.org/10.1038/nature08228
558 28. Lin, J. C., Gerbig, C., Wofsy, S. C., Andrews, A. E., Daube, B. C., Davis, K. J., & Grainger,
559 C. A. (2003). A near-field tool for simulating the upstream influence of atmospheric
560 observations: The Stochastic Time-Inverted Lagrangian Transport (STILT) model. *Journal of*
561 *Geophysical Research: Atmospheres*, 108(D16). https://doi.org/10.1029/2002JD003161
562 29. Lin, J. C., Gerbig, C., Wofsy, S. C., Andrews, A. E., Daube, B. C., Grainger, C. A., et al.
563 (2004). Measuring fluxes of trace gases at regional scales by Lagrangian observations:
564 Application to the CO_2 Budget and Rectification Airborne (COBRA) study. *Journal of*
565 *Geophysical Research: Atmospheres*, 109(D15). https://doi.org/10.1029/2004JD004754
566 30. Lin, J. C., Brunner, D., Gerbig, C., Stohl, A., Luhar, A. K., & Webley, P. W. (2012).
567 Lagrangian Modeling of the Atmosphere. *Geophys. Monogr.*, 200, 349.
568 https://doi.org/10.1029/GM200
569 31. Macatangay, R., Warneke, T., Gerbig, C., Körner, S., Ahmadov, R., Heimann, M., &
570 Notholt, J. (2008). A framework for comparing remotely sensed and in-situ CO_2
571 concentrations. *Atmospheric Chemistry and Physics*, 8(9), 2555-2568.
572 https://doi.org/10.5194/acp-8-2555-2008
573 32. Mahaffy, P. R., Webster, C. R., Cabane, M., Conrad, P. G., Coll, P., Atreya, S. K., et al.
574 (2012). The sample analysis at Mars investigation and instrument suite. *Space Science*
575 *Reviews*, *170*(1), 401-478. https://doi.org/10.1007/s11214-012-9879-z

33. Mallia, D. V., Lin, J. C., Urbanski, S., Ehleringer, J., & Nehrkorn, T. (2015). Impacts of upwind wildfire emissions on CO, CO_2, and $PM_{2.5}$ concentrations in Salt Lake City, Utah. *Journal of Geophysical Research: Atmospheres*, 120(1), 147-166. https://doi.org/10.1002/2014JD022472

34. Mischna, M. A., Allen, M., Richardson, M. I., Newman, C. E., & Toigo, A. D. (2011). Atmospheric modeling of Mars methane surface releases. *Planetary and Space Science*, 59(2-3), 227-237. https://doi.org/10.1016/j.pss.2010.07.005

35. Montmessin, F., Korablev, O. I., Trokhimovskiy, A., Lefèvre, F., Fedorova, A. A., Baggio, L., et al. (2021). A stringent upper limit of 20 pptv for methane on Mars and constraints on its dispersion outside Gale crater. *Astronomy and Astrophysics*-A&A, published online. https://doi.org/10.1051/0004-6361/202140389

36. Moores, J. E., Gough, R. V., Martinez, G. M., Meslin, P. Y., Smith, C. L., Atreya, S. K., et al. (2019a). Methane seasonal cycle at Gale Crater on Mars consistent with regolith adsorption and diffusion. *Nature Geoscience*, 12(5), 321-325. https://doi.org/10.1038/s41561-019-0313-y

37. Moores, J. E., King, P. L., Smith, C. L., Martinez, G. M., Newman, C. E., Guzewich, S. D., et al. (2019b). The methane diurnal variation and microseepage flux at Gale crater, Mars as constrained by the ExoMars Trace Gas Orbiter and Curiosity observations. *Geophysical Research Letters*, 46(16), 9430-9438. https://doi.org/10.1029/2019GL083800

38. Mumma, M. J., Villanueva, G. L., Novak, R. E., Hewagama, T., Bonev, B. P., DiSanti, M. A., et al. (2009). Strong release of methane on Mars in northern summer 2003. *Science*, *323*(5917), 1041-1045. https://doi.org/10.1126/science.1165243

39. Newman, C. E., Gómez-Elvira, J., Marin, M., Navarro, S., Torres, J., Richardson, M. I., et al. (2017). Winds measured by the Rover Environmental Monitoring Station (REMS) during the Mars Science Laboratory (MSL) rover's Bagnold Dunes Campaign and comparison with numerical modeling using MarsWRF. *Icarus*, 291, 203-231. https://doi.org/10.1016/j.icarus.2016.12.016

40. Newman, C. E., Baker, M. M., Banfield, D. J., Banks, M., Karatekin, O., Navarro, S., et al. (2020). *Using InSight Wind Data to Validate Atmospheric Models and Improve Predictions for Other Locations on Mars.* Paper presented at the AGU Fall Meeting 2020, online.

41. Oehler, D. Z., & Etiope, G. (2017). Methane seepage on Mars: where to look and why. *Astrobiology*, *17*(12), 1233-1264. https://doi.org/10.1089/ast.2017.1657

42. Oze, C., & Sharma, M. (2005). Have olivine, will gas: serpentinization and the abiogenic production of methane on Mars. *Geophysical Research Letters*, *32*(10). https://doi.org/10.1029/2005GL022691

43. Pla-García, J., Rafkin, S. C., Karatekin, Ö., & Gloesener, E. (2019). Comparing MSL Curiosity rover TLS-SAM methane measurements with Mars Regional Atmospheric Modeling System atmospheric transport experiments. *Journal of Geophysical Research: Planets*, 124(8), 2141-2167. https://doi.org/10.1029/2018JE005824

44. Putzig, N. E., Mellon, M. T., Kretke, K. A., & Arvidson, R. E. (2005). Global thermal inertia and surface properties of Mars from the MGS mapping mission. *Icarus*, 173(2), 325-341. https://doi.org/10.1016/j.icarus.2004.08.017

45. Richardson, M. I., Toigo, A. D., & Newman, C. E. (2007). PlanetWRF: A general purpose, local to global numerical model for planetary atmospheric and climate dynamics. *Journal of Geophysical Research: Planets*, 112(E9). https://doi.org/10.1029/2006JE002825

46. Stein, A. F., Draxler, R. R., Rolph, G. D., & Stunder, B. J. (2015). B., Cohen, MD, and Ngan, F.: NOAA'S HYSPLIT atmospheric transport and dispersion modeling system, *Bulletin of the American Meteorological Society*, 96, 2059-2077. https://doi.org/10.1175/BAMS-D-14-00110.1

47. Thomson, D. J. (1987). Criteria for the selection of stochastic models of particle trajectories in turbulent flows. *Journal of fluid mechanics*, 180, 529-556. https://doi.org/10.1017/S0022112087001940

48. Toigo, A. D., Lee, C., Newman, C. E., & Richardson, M. I. (2012). The impact of resolution on the dynamics of the martian global atmosphere: Varying resolution studies with the MarsWRF GCM. *Icarus*, 221(1), 276-288. https://doi.org/10.1016/j.icarus.2012.07.020

49. Webster, C. R., Mahaffy, P. R., Atreya, S. K., Flesch, G. J., Mischna, M. A., Meslin, P. Y., et al. (2015). Mars methane detection and variability at Gale crater. *Science*, 347(6220), 415-417. https://doi.org/10.1126/science.1261713

50. Webster, C. R., Mahaffy, P. R., Atreya, S. K., Moores, J. E., Flesch, G. J., Malespin, C., et al. (2018). Background levels of methane in Mars' atmosphere show strong seasonal variations. *Science*, 360(6393), 1093-1096. https://doi.org/10.1126/science.aaq0131

51. Webster, C. R., Mahaffy, P. R., Pla-Garcia, J., Rafkin, S. C., Moores, J. E., Atreya, S. K., et al. (2021). Day-night differences in Mars methane suggest nighttime containment at Gale crater. *Astronomy and Astrophysics*, 650 (2021) A166. https://doi.org/10.1051/0004-6361/202040030

52. Yung, Y. L., Chen, P., Nealson, K., Atreya, S., Beckett, P., Blank, J. G., et al. (2018). Methane on Mars and habitability: challenges and responses. *Astrobiology*, 18(10), 1221-1242. https://doi.org/10.1089/ast.2018.1917